

# Machine learning interatomic potentials for aluminium: application to solidification phenomena

Noel Jakse,<sup>1</sup> Johannes Sandberg,<sup>1,2,3</sup> Leon F. Granz,<sup>2,3</sup> Anthony Saliou,<sup>1</sup> Philippe Jarry,<sup>4</sup>  
Emilie Devijver,<sup>5</sup> Thomas Voigtmann,<sup>2,3</sup> Jürgen Horbach,<sup>6</sup> and Andreas Meyer<sup>2,7</sup>

<sup>1</sup>*Université Grenoble Alpes, CNRS,*

*Grenoble INP, SIMaP F-38000 Grenoble, France*

<sup>2</sup>*Institut für Materialphysik im Weltraum,*

*Deutsches Zentrum für Luft- und Raumfahrt (DLR), 51170 Köln, Germany*

<sup>3</sup>*Department of Physics, Heinrich-Heine-Universität Düsseldorf,*

*Universitätsstraße 1, 40225 Düsseldorf, Germany*

<sup>4</sup>*C-TEC, Parc Economique Centr'alp, 725 rue Aristide Bergès,*

*CS10027, Voreppe 38341 cedex, France*

<sup>5</sup>*Univ. Grenoble Alpes, CNRS, Grenoble INP, LIG, F-38000 Grenoble, France*

<sup>6</sup>*Institut für Theoretische Physik II,*

*Heinrich-Heine-Universität Düsseldorf,*

*Universitätsstraße 1, 40225 Düsseldorf, Germany*

<sup>7</sup>*Institut Laue-Langevin (ILL), 38042 Grenoble, France*

## Abstract

In studying solidification process by simulations on the atomic scale, the modeling of crystal nucleation or amorphisation requires the construction of interatomic interactions that are able to reproduce the properties of both the solid and the liquid states. Taking into account rare nucleation events or structural relaxation under deep undercooling conditions requires much larger length scales and longer time scales than those achievable by *ab initio* molecular dynamics (AIMD). This problem is addressed by means of classical MD simulations using a well established high dimensional neural network potential trained on a relevant set of configurations generated by AIMD. Our dataset contains various crystalline structures and liquid states at different pressures, including their time fluctuations in a wide range of temperatures considering only their energy labels. Applied to elemental aluminium, the resulting potential is shown to be efficient to reproduce the basic structural, dynamics and thermodynamic quantities in the liquid and undercooled states without the need to include neither explicitly the forces nor all kind of configurations in the training procedure. The early stage of crystallization is further investigated on a much larger scale with one million atoms, allowing us to unravel features of the homogeneous nucleation mechanisms in the fcc phase at ambient pressure as well as in the bcc phase at high pressure with unprecedented accuracy close to the *ab initio* one. In both case, a single step nucleation process is observed.

## I. INTRODUCTION

Apart from steels, aluminium and its alloys represent the most used and attractive structural metallic materials due to their specific properties such as low weight, low energy cost of remelting, and the possibility of almost complete recycling. Therefore, these materials represent a major axis of the energy transition [1]. An intimate understanding of its condensed phase properties is founded upon a description of the atomic level structure and dynamics, and requires an accurate representation of chemical bonding [2]. This is of utmost importance in order to tackle phenomena such as phase changes and solidification process during which a liquid morphs into a solid either by crystallization or amorphisation [3, 4], showing eventually a change in electronic structure as a metal-to-semiconductor transition [5, 6]. First-principles approaches, essentially through the Density Functional Theory (DFT) [7, 8], represent the dedicated framework especially with the breakthrough provided by *ab initio* molecular dynamics (AIMD) simulations [9] in combining atomic dynamics with DFT. Despite its enormous success in many complex chemical bonding environments [2], DFT implementations are limited to a few hundred atoms over time scales less than 1 ns [10, 11] on current large-scale supercomputing facilities, impeding its use for phenomena at length and time scales typical of solidification [12].

The desire to bridge typical scales of the electronic structure to those of the properties under investigation has led to deriving interatomic potentials with semi-empirical functional forms that average out or otherwise model electronic degrees of freedom. For metallic materials of interest here, various approaches were proposed, starting in the second half of the 20th Century with pair-potentials based on a nearly-free electron gas description of the electronic structure [13] using simple models within the pseudopotential theory (PT) [15–18]. It was later acknowledged that it was impossible for pair potentials to describe on the same footing the structure, dynamic, and thermodynamic properties in the liquid and solid state [14], with inherent mechanical instability under shear for crystals. Many-body approaches such as the Embedded-Atom Model (EAM) [19, 20], modified EAM (MEAM) [21] of current widespread use as well as the Reactive Force Field (ReaxFF) [22], just to name a few among many others [23], can be considered as successful in this respect. Fitting the parameters of

these potentials is most often oriented towards describing crystalline phases and transitions between some of them [25, 26], more rarely taking a full account of the liquid state [24]. This leads to a lack of transferability [14] and a limited ability to tackle phenomena involving several phases such as crystal nucleation [12].

Over the last decade, impressive progress was made in designing potentials from electronic structure calculations using supervised Machine Learning (ML) methods [27–33]. There are now standard libraries for the ML training [34] that can be used in combination with molecular dynamics (MD) simulation packages [35] such as LAMMPS [36] or in combination with workflow environments such as ASE [37]. On-the-fly ML force field methods have been also proposed [38] and implemented directly into *ab initio* codes in order to bypass most of electronic-structure calculation steps [39]. Different ML techniques have been used, ranging from simple linear regression (LR) methods such as the spectral neighbor analysis potential (SNAP) method [31, 42] to highly non-linear regression methods using High Dimensional Neural Networks [34, 40] (HDNN) or Kernel Regression (KR) [41, 43, 44]. The designed potentials reach in general an accuracy close to the *ab initio* calculations from which the database was formed, with exceptional results for the description of relative stability between crystalline phases [46] and defects [26]. However, approaches taking full account of liquid and crystalline states remain scarce [6, 46, 47] and are often limited to the objective of a good description of the melting point. The main reason for this stems from the fact that the chosen *ab initio* configurations should cover all situations, as ML techniques may become less reliable outside the training domain [27]. It becomes even more crucial for crystal nucleation occurring under deep undercooling conditions with a strong evolution of the liquid structure with respect to that above melting, showing an increasing icosahedral [10] ordering and structural heterogeneity [48] triggering homogeneous nucleation [49].

Machine-learning potentials for aluminium were designed very recently to describe essentially the properties of the solid states [47, 50, 51] and the melting temperature [47, 50], but none of them taking the liquid structure and dynamics fully into account. Two different approaches were put forward respectively with a Gaussian kernel regression [50] and a deep NN [51] with a dataset built from configurations extracted from AIMD simulations at various temperatures. ML potentials were initially trained using the DFT energies starting from

the work of Behler and Parrinello on bulk Si [40]. It was subsequently pointed out that the learning process could benefit from a wealth of additional information if the three components of the force and six components of the stress per atom are taken into account [27, 33], while one has only a single energy value per simulated configuration. Still in some works, only the forces have been used for the training showing that properties like the vibrational properties in the solid states can be reproduced, but they remain insufficient to get full account of thermodynamic quantities [44, 50]. Thus whether additional information enhances the training or not can still be questioned, also given the fact that the relative importance of the energy, forces and stresses for estimating the Mean-Square Error (MSE) or the Root-MSE (RMSE) introduce two additional free training parameters [27]. Moreover, the question of the transferability of a ML potential taking into account both the liquid and solid phases as mentioned above, remains essentially unexplored for aluminium. This aspect is also of importance when dealing with solidification phenomena.

The aim of the present work is to develop a ML potential for pure aluminium dedicated to the description of condensed phases, namely liquid and solid states for temperatures up to 8000 K and pressures up to 300 GPa. For this purpose, a HDNN was developed on the basis of well-known and robust Behler and Parrinello’s approach [27, 40]. The latter was trained on a data set generated by DFT-based simulations for the main crystalline structures and liquid states covering the targeted pressure and temperature domain, including their time fluctuations by an appropriate sampling of phase space trajectories [85]. It is shown that training the HDNN on sampled AIMD trajectories using solely energy labels leads to an accurate description of the structure, dynamics and thermodynamics in the investigated domain. More specifically, the single-particle as well as the collective dynamics are well reproduced, which is an essential ingredient in describing solidification. The resulting potential is then applied here to solidification processes, namely amorphisation and early stages of crystal nucleation, allowing us to unravel features of the homogeneous nucleation mechanisms at ambient as well as high pressure.

The remaining part of the paper is organized as the following. In Sec. II, the specific features of the HDNN, the training procedure as well as the basic assessment of the potential on independent DFT and experimental thermodynamic data are outlined. Sec. III is devoted

to the test of the potential’s accuracy in describing some structural properties, the dynamics of the liquid state in the investigated pressure-temperature domain, as well as the homogeneous nucleation. Finally, in Sec. IV, the main outcomes of the work are given.

## II. COMPUTATIONAL BACKGROUND

### A. Constructing a machine learning potential

In the last three decades, many potentials of pure Al and its alloys for the use in atomistic simulations been developed [1, 2, 52–57, 59, 60, 62–65], using the Morse potential ansatz [52], the PT method [60], embedded-atom method (EAM) [2, 54–56, 59, 63], the modified EAM (MEAM) [1, 21, 65], and many-body approaches such as COMB3 [64]. However, only very few studies have employed the ML approach [44, 50, 51], none of them taking systematically into account the properties of the liquid state and checking the dynamics which is very important for the solidification aspects. This is precisely one of the aims in building a ML-based potential here.

Among the various approaches put forward to design ML potentials [28, 31], the choice was made to set up a high-dimensional neural network built in a similar way to the one proposed by Behler and Parrinello [40] and Zhang *et al.* [66]. This well established approach has been proven successful for pure silicon [6] as well as water [46] to model reliably both their properties in the liquid and solid states. As a detailed description can be found for instance in the tutorial review by Behler [27] among others, the focus is made mainly on the specifics of our scheme. The main part consists in a supervised learning task from a relevant sample of atomic configurations with known energy generated by AIMD in various crystalline and liquids structures in the desired temperature and pressure domain. In the corresponding portion of Potential Energy Landscape (PEL), each configurational energy is considered as a sum of individual atomic energies determined from their local atomic environment within a cut-off radius  $r_S$  often extending beyond the first-neighbor atomic shell, and taken here to be 6.4 Å for Al, corresponding to at least the second neighbor shell for all the considered thermodynamic states. This decomposition allows us to train  $N$  Neural Networks (NN),

each of them being assigned to an individual local atomic environment. The NN are then combined to recover the energy of the whole configuration of  $N$  atoms.

The individual NN is defined by the same network topology for given atomic species. It specifies the number of neurons formally named here  $y_i^l$  and their connectivity through the weights,  $w_{i,j}^l$ , and called a Multi-Layer Perceptron (MLP). The weights associated with each node pair are optimized during the learning process by a back-propagation technique [67]. Thus, each of the  $M$  layers within the neural network consists of sets of nodes receiving multiple inputs from the previous layer and passing outputs to the next layer. Here a fully connected network is used, in which every output of a layer is an input for every neuron in the next layer. The corresponding mathematical description is as follows: the input signals are linearly combined before being activated by function  $f$  to give each output  $y_i^l$  of a given fully connected layer  $l$  as

$$y_i^l = f \left( \sum_{j=1}^{M_{l-1}} w_{i,j}^l y_j^{l-1} + b_i^l \right), \quad (1)$$

where  $M_l$  refers to the size of the  $l$ -th layer, *i.e.* the number of its neurons. Note that positive weights enhance connections while negative weights tend to inhibit them. Most of the activation functions are chosen to have a range in either  $[0, 1]$  or  $[-1, 1]$  and modulate the amplitude of the output. The activation function  $f$  is applied element-wise and is taken as the softplus function  $f(x) = \log(1 + e^x)$ . Back-propagation is used to update the network weights and their gradients.

The input layer of a NN takes values representative of one local atomic environment in the form of a feature vector whose dimension is then equal to the number of its nodes. The feature vector is built on the basis of Behler-Parrinello (BP) descriptors [40] to represent the radial and angular arrangements of atoms in the local structure using Gaussian symmetry functions having the translational and rotational invariance. For aluminium, the number of components of the BP feature was chosen to be 22, comprising of 12 radial and 10 angular components, as described in more detail in the Supplementary Information (SI) file. Then, the NN architecture for aluminum is  $22 \times 10 \times 10 \times 1$  with 2 hidden layers of 10 nodes each.

The NN was coded using KERAS module from the TENSORFLOW PYTHON package [68] in the regression mode. NNs of all  $N$  atoms of a configuration are then associated using the

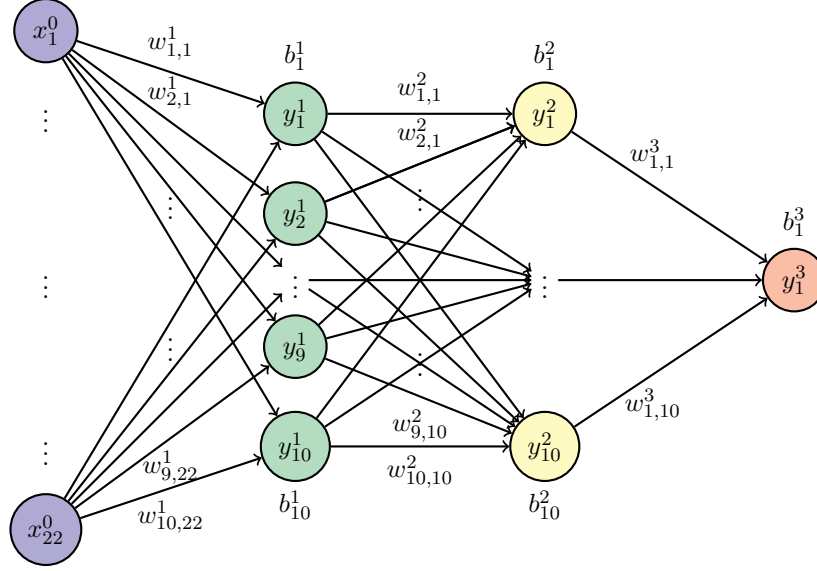


FIG. 1. Schematic representation of the feed-forward neural network built as a densely connected multi-layer perceptron. The input layer  $x_i^0$  will be fed with the atomic BP feature of the training set, and the output is the atomic energy. The neural network contains two hidden layers with superscript 1 and 2, respectively. The two layers are composed of 10 neurons each. The weights  $w_{ij}^k$  and bias  $b_i^k$  are optimized during the training (see text).

ADD module to form the HDNN which is obviously invariant to permutation of atoms. The HDNN is then trained on the single DFT energy of the whole configuration.

## B. Building the dataset

Designing an appropriate dataset is the crucial and demanding step for the construction of the NN interatomic potential. Various strategies can be put forward to construct it, which were reviewed very recently [69]. Here, it was built from AIMD simulations that were partly taken from our previous works [10, 70–72] and extended here to have a better representation of the undercooled liquid region, the crystalline fcc configurations up to the melting point at zero pressure, and crystalline fcc, bcc, and hcp up to 300 GPa with and without defects. The different thermodynamic states and structures as well as the number of configurations sampled in each case are given in Tables SII and SIII in the Supplementary Information



file. In total, 24300 configurations of  $N = 256$  atoms were gathered in the database that enabled us to cover solid and liquid states at ambient pressure as well as liquid samples at temperatures up to 8000 K and pressures up to 300 GPa. Non-equilibrium trajectories in the undercooled region were also generated to take into account crystal nucleation and solidification processes in the ML fitting procedure.

For the sake of self-consistency, the main technical details of the AIMD simulations are recalled here. They were performed by means of the Vienna Ab initio Simulation Package (VASP) [73]. The local density approximation (LDA) [74, 75] within projected augmented plane-waves was applied to all simulations with a plane-wave cutoff of 241 eV. For the liquid states, only the  $\Gamma$ -point is used while for crystalline states, the  $\Gamma$ -centered grid of  $k$ -points in the irreducible part of the Brillouin zone was set to  $2 \times 2 \times 2$  following the Monkhorst–Pack scheme [77, 78]. All the simulations were performed with  $N = 256$  atoms placed in a cubic simulation box (except for the hcp crystal where an orthorhombic box was used) with standard periodic boundary conditions (PBC). Newton’s equations of motion were solved numerically with Verlet’s algorithm in the velocity form with a time step of 1.5 fs, and phase-space trajectories were constructed within the canonical ensemble (NVT), by means of a Nosé thermostat to control the temperature  $T$ . The temperature evolution in the undercooled states was obtained by quenching the system stepwise down to 600 K with a temperature step of 50 K. For each temperature, the simulation cell was resized according to the experimental density [79] and the run was continued for 30 ps before performing the next quench, resulting in an average cooling rate of  $3.3 \times 10^{12}$  K/s. The calculated pressures for all the temperatures studied here were in the range  $\pm 1$  GPa generally, so that on average a quasi constant pressure during the quenching is observed. For temperatures ranging from  $T = 1000$  K to 600 K, the run was continued for equilibration during a time up to 200 ps. A similar procedure was applied for heating the fcc crystal from 10 K to 900 K.

Several aspects deserve attention in the perspective of building the ML potential. First of all, the choice of the exchange and correlation (XC) functional for the electronic structure calculations is crucial. As the ML potential may reach an accuracy similar to the DFT calculations, it will mirror the ability of the XC functional used in predicting the properties, at least in the thermodynamic domain inside which it was trained. This has guided our choice

of the Local Density Approximation (LDA) functional given the fact that the Generalized-Gradient-Approximation (GGA) overestimates the atomic volume [81]. Moreover, it was shown in our previous contributions that the LDA gives a good description of the liquid structure [10]. More importantly, atomic transport properties such as the self-diffusion coefficient, which are very sensitive to the details of the potentials, are well reproduced within the LDA compared to state-of-the-art experimental data [80, 82]. Such a good agreement with experiments was very recently confirmed on the dynamic structure factors as well as the structural relaxation times extracted from the intermediate scattering function [72]. For high pressures, it was shown [83] that the difference between LDA and GGA [84] is negligible in describing the pressure-density phase diagram of aluminium up to pressures as high as 10 TPa.

Secondly, in the perspective of performing MD simulations, care has to be taken in describing not only average thermodynamic properties but also the fluctuations around the mean value, especially in order to capture the features of local basins of the PEL [85]. This requires the sampling of a large number of configurations along AIMD phase space trajectories. Therefore, in the present work, for each of the considered thermodynamic states (see Tables SII and SIII of the SI file), 1000 configurations were generated on AIMD production runs over 40 ps.

Finally, as mentioned in the introduction, the question whether including the additional information of the forces or even the stresses in addition to the energies improves the learning process and the accuracy of the potential deserves further attention. It was shown very recently for molecular systems that forces and energies contribute equally to the convergence of the prediction errors [86]. The choice of considering energies, forces or both of them in the training may depend on factors such as the application domain, the properties of interest, the complexity of the ML tool, and the strategy in building the data from *ab initio* calculations. When making static DFT calculations on chosen configurations, including forces and/or stresses labels make more sense, especially when augmentation of information is performed by generating configurations from it by random atomic displacements. Here a strategy solely based on energy labels for the training is chosen since the data consists of sampled AIMD trajectories for each thermodynamic state whose accessible microstates explore, through

the thermal fluctuations, their local basin of the PEL, taking implicitly their gradients into account [85].

### C. Training the Neural Network

The supervised training is carried out using as input the BP feature vectors describing local atomic environments in each configuration. AIMD energies of these configurations are used to find the optimal set of weights and biases. The complete dataset of configurations is firstly randomized and scaled using the standard scaler of SCIKIT-LEARN, *i.e.* centering the feature components about their mean and normalize them according to their standard deviation. It is then split into a training set of 80% of the data and a test set containing the 20% remaining part. In the training set 20% of the data are retained further to create validation sets. They are used (i) for a cross-validation procedure to estimate the performance of various NN architectures through the MSE, and (ii) to monitor the MSE on the validation data during the learning process to detect overfitting. For a given architecture, the optimization is performed using the training data without the validation set, and terminating when the validation error starts to increase. Reduction of the noise of the MSE during training is obtained by including a callback with a stepwise reduction of the learning rate. Simultaneously, a  $L_2$  norm regularization with strength  $10^{-5}$  is performed to reduce the model complexity, and thus to prevent overfitting. Once trained, the weights and biases are stored in a format compatible with the LAMMPS HDNNP pair-style [35].

This training stage is repeated with various NN architectures to find the optimal one capturing at best the functional dependence of the data. Evaluation of the MSE is carried out through a stochastic gradient descent minimization using the Adam optimization algorithm [67] giving a measure of the loss with a learning rate starting at 0.01 and reducing most of the time to 0.0001 during the training,  $\beta_1 = 0.9$ ,  $\beta_2 = 0.999$  and  $\varepsilon = 10^{-8}$ . The early-stopping was performed with maximum loss variation of  $10^{-6}$  and a patience of 45 epochs. The typical duration of the training period was about 10000 to 15000 epochs. The least MSE loss is obtained for an architecture of 10 neurons in the first and second hidden layers. A typical evolution of loss and the validation loss is shown in Fig. 2(a). A cross-validation performed

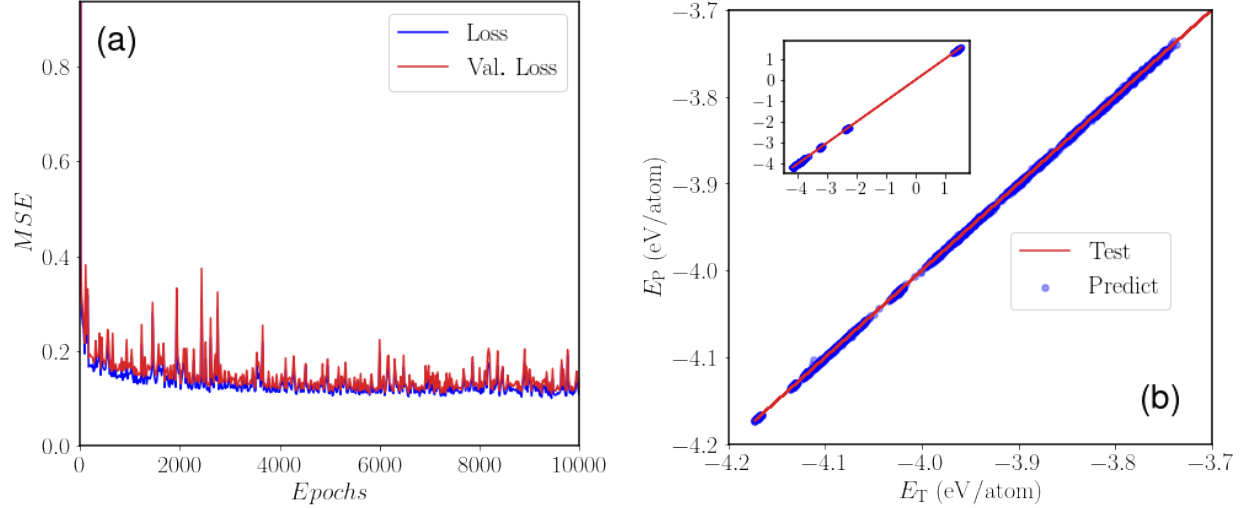


FIG. 2. (a) Evolution of the MSE losses as a function of number of epochs for the training and validation sets. Loss and Val. Loss correspond to the evaluation of the MSE on the training set and validation set, respectively. (b) Test-Predict curve showing the quality of the prediction on the test set for the optimized architecture  $22 \times 10 \times 10 \times 1$ . The red solid line represents the known output of the energies representing the know  $E_T = E_T$  line that would correspond to a perfect prediction, and the blue dots the values predicted against the known ones. The main panel corresponds to thermodynamic states at low pressures ( $< 5$  GPa) and temperatures between 10 K and 1500 K containing either crystalline and liquid configurations. The inset corresponds to energies in the full range of temperatures and pressures (see text).

over 5 independent trainings gives a RMSE of (1.2) meV on the per atom energy. Figure 2(b) displays the predictive ability of the model on the unseen data of the test set, with a high quality over the whole range of the energies.

The predictive ability of the HDNN is illustrated in Fig. 3 on the three forces components extracted from AIMD configurations of a simulation at 1500 K over 2 ps, with a RMSE of  $0.074 \text{ eV}/\text{\AA}$  at this high temperature. At  $T = 10 \text{ K}$  in similar sampling conditions the RMSE reduces to  $0.030 \text{ eV}/\text{\AA}$ . These RMSE values are consistent with those obtained for previous trained ML potentials for Al for which forces were included explicitly in the training [50, 51]. Our results lead to similar conclusions for molecular systems [86] saying that the forces can be

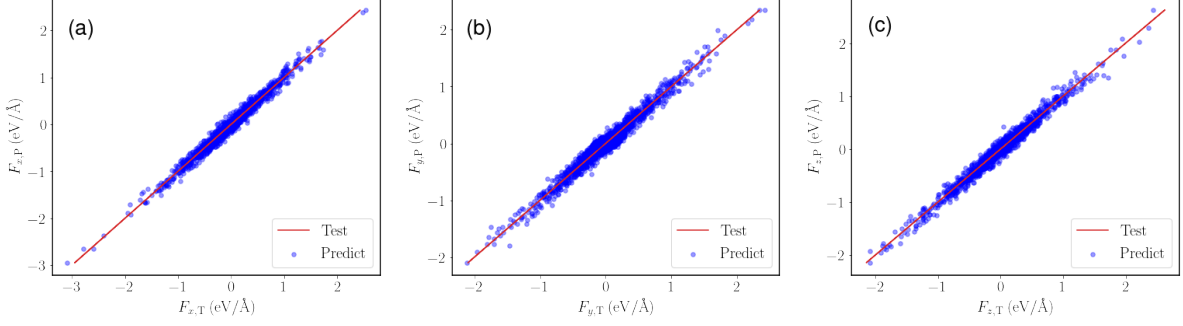


FIG. 3. Test-Predict curves for the three components of the predicted forces against those extracted from the AIMD configurations at  $T = 1500$  K over 2 ps. The red solid line and blue dots have the same meaning as in Fig. 2.

predicted with a good accuracy without being explicitly part of the learning process, and thus is in favor of the supervised learning strategy based only on the energy of the configurations, thus avoiding additional parameters in the loss function.

The HDNN is further tested on the prediction of the energy as a function of time. Consecutive configurations of AIMD simulation of liquids were considered at  $T = 600$  K in the undercooled region,  $T = 950$  K in the vicinity of the melting point, at 1500 K far above the melting point at zero pressure, and  $T = 8000$  K just above the melting line for a pressure of 322 GPa, as show in Fig. 4. Energy fluctuations are very well reproduced for all the temperatures, even for the extreme values for which the sampling is scarce, as they correspond to the tail of the Gaussian distribution of energy fluctuations. Probably the most impressive agreement is that of the simulation at  $T = 8000$  K where the energy range of the fluctuation is as large as 0.25 eV/atom and still very well predicted. This demonstrates the quality of the ML potential.

#### D. Molecular dynamics simulation

Classical MD simulations were carried out using the LAMMPS package [36]. These simulations were performed in various ensembles, namely the canonical ensemble ( $NVT$ , constant temperature, volume, and number of atoms), the isobaric-isothermal ensemble ( $NPT$ ,

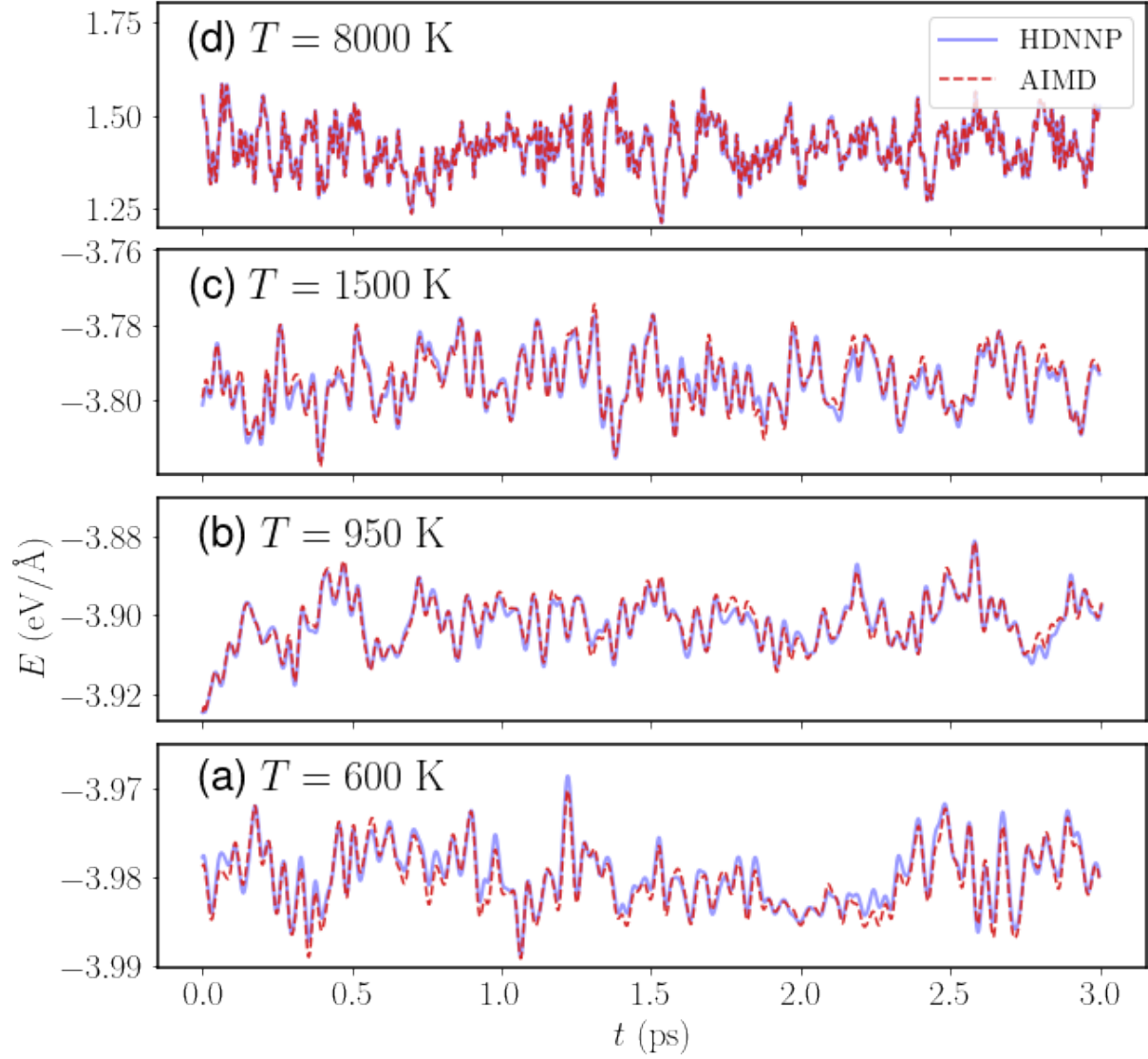


FIG. 4. Energy per atom as a function of time from AIMD simulation of liquids and predicted by the HDNN potential at  $T = 600$  K in the undercooled region,  $T = 950$  K in the vicinity of the melting point, at  $1500$  K far above the melting point at zero pressure, and  $T = 8000$  K just above the melting line for a pressure of  $322$  GPa.

constant temperature, pressure, and number of atoms), and the isobaric-isoenthalpic ensemble (NPH, constant pressure, enthalpy, and number of atoms). Temperature and pressure were kept constant *via* the Nose-Hoover thermostat and barostat [87, 88], respectively. In all simulations, PBC were employed in the three spatial directions. The integration of the equations of motion was done *via* Verlet’s algorithm in the velocity form, choosing a time step of 1 fs. The use of our HDNN potential in LAMMPS was possible through the library-based implementation of high-dimensional neural network potentials by Singraber *et al.* [35]. To assess the quality of our HDNN potential, some of the MD simulations were also repeated with the previously published ANI-Al potential of Smith *et al.* [47].

Structural analysis is performed using the common-neighbor analysis (CNA) [92] with the indexing of Faken and Jonsson [93] and a bond-based algorithm as implemented in the OVITO software [94] where a uniform cut-off radius corresponding to the first minimum of the pair-correlation function of the liquid is applied to create bonds between pairs of particles. The CNA classifies pairs around each atom by sets of three indices: the first index represents the number of nearest-neighbors common to this pair, the second index corresponds to the number of nearest-neighbor bonds among the shared neighbors, and the third index indicates the longest chain of bonded atoms among them. For instance, 421 and 422 bonded pairs are characteristic of close packed structures fcc and hcp, respectively. The occurrence of 444 and 666 pairs, with specific proportions, signals the presence of bcc ordering. The degree of five-fold symmetry is obtained from the proportion of 555, 554 and 433 pairs, which represent perfect (555) and distorted FFS based motifs.

An alternate way of studying the local ordering before and during nucleation is to make use of the Steinhardt bond-ordering parameters[4]. More specifically, the averaged form[5] as implemented in the PYSCAL code [6] is considered here. First, for each atom  $i$ , the following vector is define

$$q_{lm}(i) = \frac{1}{N(i)} \sum_{j=1}^{N(i)} Y_{lm}(\mathbf{r}_{ij}) \quad (2)$$

where  $N(i)$  is the number of nearest neighbors of atom  $i$ ,  $\mathbf{r}_{ij}$  is the displacement of nearest-neighbor atom  $j$  from  $i$ , and  $Y_{lm}$  is the spherical harmonics. From these, the averaged

bond-order parameters can be defined as

$$\bar{q}_l(i) = \sqrt{\frac{4\pi}{2l+1} \sum_{m=-l}^l \left| \frac{1}{N(i)+1} \sum_{k=0}^{N(i)} q_{lm}(k) \right|^2} \quad (3)$$

where the sum from  $k = 0$  to  $N(i)$  includes both the atom  $i$  and its nearest neighbors. Due to being averaged over nearest neighbors, these parameters take into account not just the first coordination shell, but also the second one. To perform structural analysis using these parameters one typically selects specific values for  $l$ , with  $l = 4$  and  $l = 6$  being a common choice. It is then possible to compare the resulting values of  $\bar{q}_l$  to those of ideal crystals in order to identify crystal structure.

### III. RESULTS AND DISCUSSION

#### A. Local structure and dynamics

In a first step, the optimized HDNN potential is assessed on the local structure and dynamics. The simulations are performed at a constant volume, given in top row of Table I, with  $N \simeq 10000$  atoms at selected temperatures. For the undercooled states the system is first prepared at a temperature of 1500 K, before being cooled down to the desired temperature. The other states are prepared directly at the target temperature from a fully equilibrated liquid. Following an equilibration time of 10 ps relevant quantities are calculated over a production time ranging from 100 ps to 1 ns depending on the thermodynamic state under consideration.

The pair-correlation function  $g(r)$  gives the probability of finding a particle  $j$  at distances  $r_{ij}$  relative to a particle  $i$  located at the origin, and reads:

$$g(r_{ij}) = \frac{N}{V} \frac{n(r_{ij})}{4\pi r_{ij}^2 \Delta r}. \quad (4)$$

$n(r)$  represents the mean number of particles  $j$  in a spherical shell of radius  $r$  and thickness  $\Delta r$  centered on particle  $i$ . Finally, an average of  $g(r)$  over all  $N$  particle  $i$  of the simulation box is performed. Integrating  $4\pi r^2 \rho g(r)$ , with  $\rho = N/V$  up to the first minimum  $g(r)$  gives access to the mean coordination number. Figure 5 displays the curves of  $g(r)$  from  $NVT$



simulations. An excellent match with AIMD simulations is seen for all the thermodynamic states. A quantitative estimation of the deviation was obtained by calculating the MSE between the classical MD and AIMD curves for each temperature. The MSE ranges from  $6 \times 10^{-4}$  typically in the case of the liquid states to  $1.2 \times 10^{-2}$  in the case of fcc solid states. The larger MSE for the solid might come from the fact that even a very small position shift of  $g(r)$  can induce a significant deviation as peaks are sharp and narrow. The curves of  $g(r)$  obtained from the ANI-Al ML potential of Smith *et al.* [47] are slightly shifted to larger distances for all liquid states considered, thus overestimating the bond lengths, and their peaks in the crystalline states are more pronounced. The average coordination numbers with the HDNN potential display a deviation from AIMD that does not exceed 0.2 (see Table I). Nevertheless, a comparison of  $g(r)$  of the present HDNN potential to those obtained with published ML potentials is considered. Fig. 5(c) shows that our potential leads to overall better results than the ML potential of Kruglov *et al.* [50] as compared to their *ab initio* simulations and experimental data at  $T = 1000$  K. In Fig. 5(d) our potential leads to results very close to the recent ANI-Al potential of Ref. [47], and in good agreement with experiments [96] at  $T = 1123$  K,  $T = 1183$  K and  $T = 1273$  K. It is worth mentioning that both mentioned ML potentials have been trained using only the forces [50] or using the energies and forces [47], contrary to the present potential. Additional comparison with the most widely used EAM [2] and MEAM [1] potentials is shown in Fig. S1 in the Supplementary Information File for the same thermodynamic states. They are shown to perform less well than the HDNN potential, as assessed by a  $t$ -statistics, and especially for the high pressures.

Beside the local structural properties, dynamic properties represent a stringent test as they are even more sensitive to the details of the potentials. Among these, diffusion plays an important role in the solidification process [12, 95] and was evaluated here through the mean-square displacement (MSD)

$$R^2(t) = \frac{1}{N} \sum_{l=1}^N \left\langle [\mathbf{r}_l(t + t_0) - \mathbf{r}_l(t_0)]^2 \right\rangle_{t_0}, \quad (5)$$

where  $\mathbf{r}_l(t)$  denotes the position of atom  $l$  at time  $t$  and  $N$  is the number of atoms. In addition to the mean over all atoms, an averaging over time origins  $t_0$  as indicated by the angular brackets is performed. The self-diffusion coefficient  $D$  is determined from the slope of the

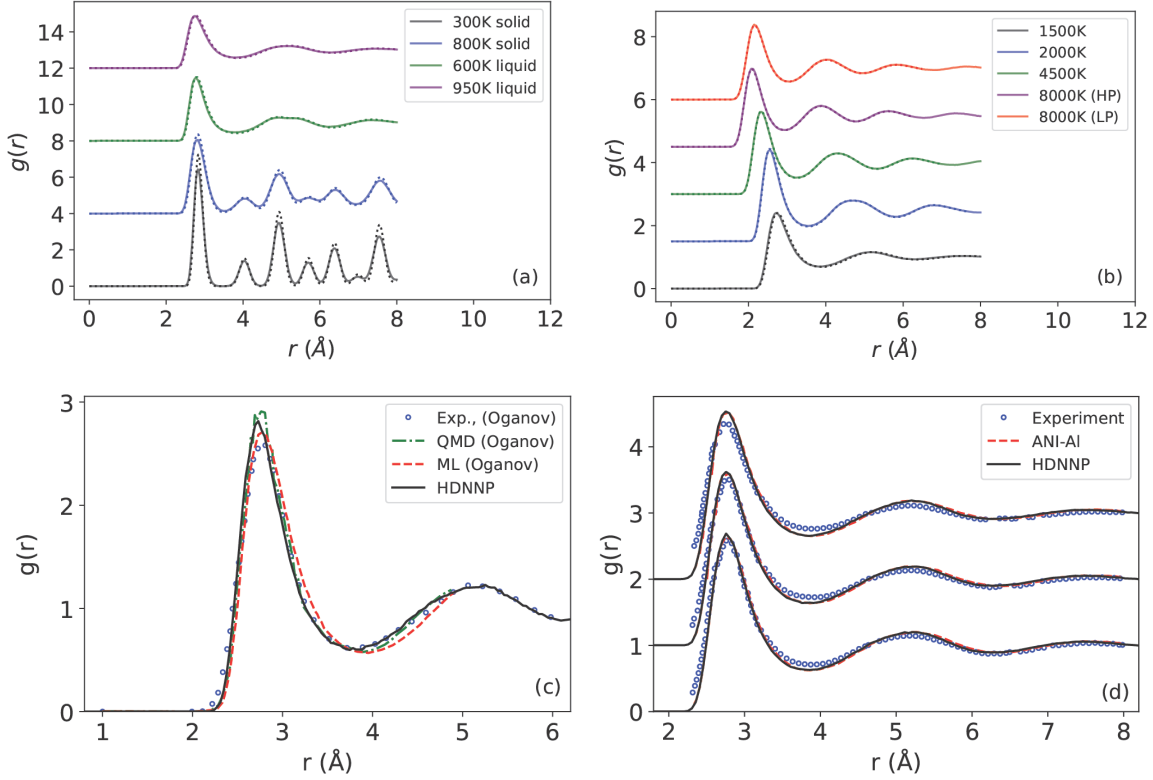


FIG. 5. Pair-correlation function for various temperatures and pressures (a) for low temperature liquid and solid states at room pressure and (b) for high temperature and pressure liquid states. Curves for 800 K, 600 K, 950 K, 2000 K, 4500 K, 8000 K (340 GPa) and 8000 K (240 GPa) are shifted upwards by an amount of 4, 8, 12, 1.5, 3, 4.5 and 6, respectively. The solid lines are results with the HDNN potential, the dotted lines to the ANI-AI potential, and the dashed lines with corresponding colors are those of the AIMD simulations. (c) Comparison in the liquid at  $T = 1023$  K to simulations with the ML potential of Ref. [50] as well as their *ab initio* calculations and experimental data. (d) Comparison in the liquid at  $T = 1123$  K,  $T = 1183$  K and  $T = 1273$  K to simulations with the ANI-AI potential of Ref. [47] as well as experimental data of Ref. [96].

linear behavior at long times of the MSD. In Fig. 6, the MSD is shown for temperatures in the stable and undercooled liquid states at ambient pressure as well as for temperatures along the melting line for pressures up to 340 GPa. The overall trends of AIMD curves are well reproduced by the HDNN potential for all temperatures and pressures as can be

$T(K)$	300 (s)	600	800 (s)	950	1500	2000	4500	8000 (H)	8000 (L)
$V (\text{\AA}^3)$	16.48	18.06	16.68	18.89	20.37	14.00	10.67	7.629	8.616
$P$ (GPa)	0	0	0	0	0	30	110	240	340
	0	0	0	0	0	27	107	227	320
$N_C$	-	11.93	-	11.57	11.10	12.22	12.70	12.70	12.65
	-	12.05	-	11.65	11.17	12.32	12.80	12.80	12.75
$D (\text{\AA}^2/\text{ps})$	-	0.15	-	0.63	1.69	0.35	0.78	1.01	1.35
	-	0.14	-	0.62	1.61	0.37	0.68	0.93	1.34
	-	(0.10)	-	(0.46)	(1.54)	(0.33)	(0.66)	(0.96)	(1.38)

TABLE I. Atomic volume  $V$ , pressure  $P$ , coordination number  $N_C$ , and diffusion coefficient  $D$  for selected temperatures. Values in second rows are from the AIMD, and those in parenthesis are the diffusion coefficient calculated from the ANI-Al potential [47]. Classical MD simulations for the diffusion were performed with  $N = 256$  atoms as for the AIMD one in order to have similar finite size effects. (H), (L), and (s) specifies high and low pressure, and solid state simulations respectively.

seen in Table I. It is worth mentioning that our potential gives a better prediction of the diffusion coefficients than the ANI-Al potential at ambient pressure and low temperatures where solidification phenomena occur. The MSD curves show a ballistic regime at very short times ( $t < 0.05$  ps), followed by a diffusive regime at long times. For the lower temperatures at ambient pressures and at high pressures a well-known caging effect [95] takes place after the ballistic motion and delays the diffusive regime, which is well predicted by the HDNN potential with respect to the AIMD.

The collective dynamics is examined by means of the Intermediate Scattering Function (ISF)  $F(Q, t)$  and its time Fourier transform  $S(Q, \omega)$ , the dynamic structure factor that can be measured by means of Neutron Diffraction.  $Q$  represents the wave-number and  $\omega$  the frequency. Fig. 6(c) shows the good agreement of the ISF between the HDNN potential and the AIMD results in the liquid state at  $T = 950$  K and  $T = 1300$  K for  $Q_0 = 2.65 \text{\AA}^{-1}$  corresponding to the position of the first maximum of the static structure factor  $S(Q)$ .

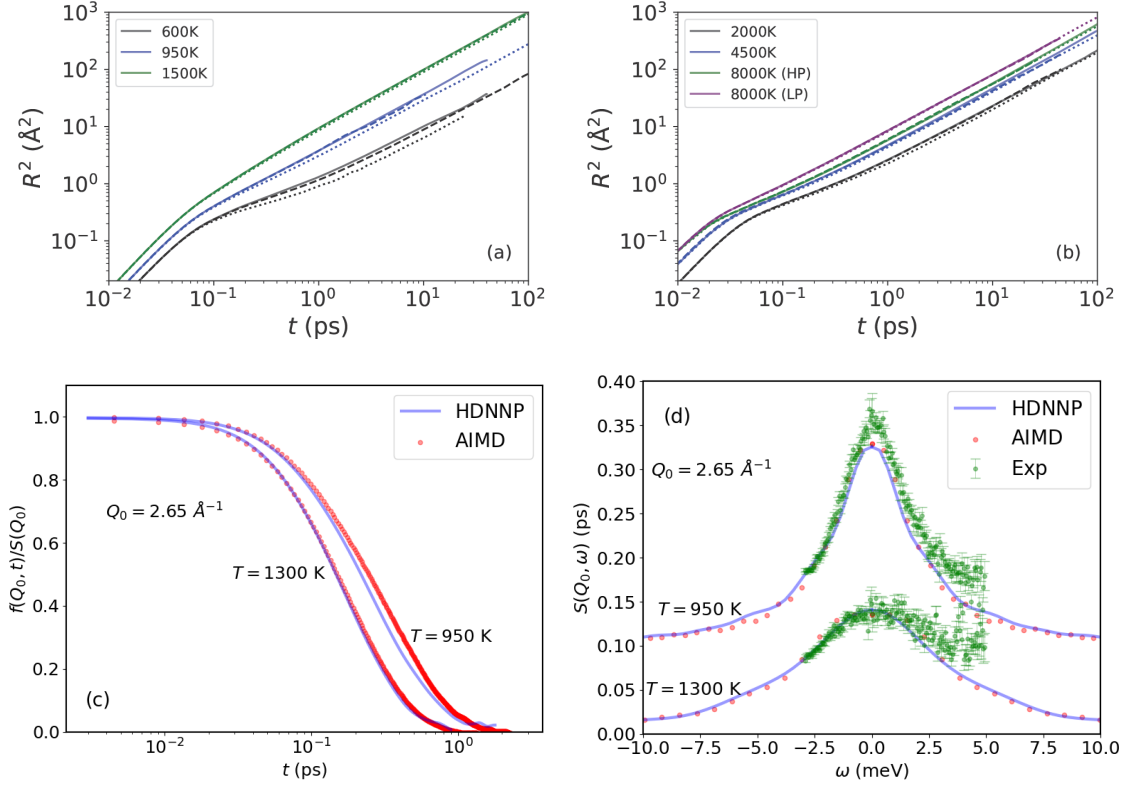


FIG. 6. Mean-square displacement for various temperatures and pressures: (a) for high temperature and pressure liquid states and (b) for low temperature liquid and solid states at room pressure. The solid lines correspond to the HDNN potential, the dotted lines to the ANI-AL potential [47], and the dashed lines are the AIMD simulations. Classical MD simulations for the MSD were performed with  $N = 256$  atoms as for the AIMD one in order to have similar finite size effects. (c) Intermediate scattering function in the liquid state at  $T = 950 \text{ K}$  and  $T = 1300 \text{ K}$  for wave vector  $Q_0 = 2.65 \text{ \AA}^{-1}$ . (d) Corresponding dynamic structure factor at the same temperatures and wavevector that are compared to the neutron diffraction experiments at  $T = 943 \text{ K}$  and  $T = 1293 \text{ K}$  from Ref. [72].

The good match is confirmed for  $S(Q, \omega)$  in Fig. 6(d) for both temperatures. Further, the comparison with Neutron diffraction data [72] demonstrates that the *ab initio* calculations as well as the HDNN potential predict the dynamic properties of liquid aluminium quite accurately.

The real predictive character of the HDNN potential is assessed for  $T = 950 \text{ K}$ ,  $T = 2000 \text{ K}$

and  $T = 8000$  K at the lowest pressure: These thermodynamic states were not included in the training, but the accuracy is similar to the other states for the pair-correlation function and the diffusion. This is all the more true for results at  $T = 1123$  K,  $T = 1183$  K,  $T = 1273$  K and  $T = 1300$  K for the comparison with other ML potentials and experiments in Figs. 5 and 6, as well as for the pressure for all states shown in Table I with a deviation less than 7% at the highest ones, which is remarkable since the forces were not included in the training.

## B. Thermodynamic properties

Important quantities for solidification phenomena are the latent heat of fusion [97, 98] as well as the densities of the solid and liquid phases at the melting temperature,  $T_M$ . Its determination requires the calculation of the enthalpy difference between the liquid and solid branches at  $T_M$ . The temperature evolution of the enthalpy at ambient pressure for the solid and liquid branches of the HDNN potential are shown in Fig. 7(a), obtained *via* simulation of  $N \simeq 2000$  atoms in the NPH ensemble. The simulation is started with a perfect fcc crystal at  $T = 300$  K and heated stepwise with a temperature step of 50 K with an average heating rate of  $10^{12}$  K/s. At each temperature, a simulation is performed over 50 ps (25 ps equilibration and 25 ps production) during which an average value of the enthalpy is calculated. The increase of temperature is repeated until a dynamic melting is observed at  $T = 1250$  K. The latter value is noticeably higher than the thermodynamic melting temperature  $T_M = 970$  K obtained from LSI simulations due to overheating effects. For the liquid branch, the simulations are started at  $T = 1600$  K with an equilibrated configuration after the heating process. The same procedure as for the solid branch is followed but with a step-wise cooling down to 300 K that is called here the slow cooling. Above  $T = 1250$  K, the difference in the enthalpy from the heating and cooling processes is negligible, indicating that there is no reminiscence of the crystalline state. Below 600 K the liquid undergoes a partial crystallization during cooling. Then, the cooling procedure for the liquid branch is repeated with a higher cooling rate of  $10^{13}$  K/s to avoid crystallization, and a glass transition is seen at  $T_G = 378$  K inferred from a crossover between the liquid and glassy branches as shown in Fig. 7(a).

For such a high cooling rate of  $10^{13}$  K/s, the time to reach each temperature is shorter than its corresponding nucleation time. This is illustrated from the time temperature transition (TTT) curve plotted in Fig. 7(b). It is determined for a system of approximately 1 million atoms (see Sec. IIID) by measuring the time it takes until 40% of the atoms are identified as in a solid state by CNA. At 600 K, the measurement is repeated from the initial configuration, but with new velocities picked from a proper Maxwell distribution, to estimate the variability between measurements.

From the liquid and solid branches an enthalpy of melting of 11.67 kJ/mol is found, which compares reasonably well to the experimental value of 13.34 kJ/mol [99]. Taking the numerical derivative of the solid branch yields a value of the specific heat at constant pressure,  $C_P$ , of 0.99 J/g/K which is also in good agreement with the experimental value of 0.91 J/g/K. For the liquid a value of 1.158 J/g/K is obtained, which is in the range of experimental data between 1.03 J/g/K and 1.18 J/g/K close to the latest assessed values of 1.127 J/g/K [99]. The specific heat is a typical derivative quantity that depends on the fluctuations of the enthalpy [87, 88]. The very good agreement is a strong indication that including the time fluctuations from AIMD is a fruitful strategy to describe at least the thermodynamics.

Regarding densities, the HDNN potential gives a value of  $0.0587 \text{ \AA}^{-3}$  and  $0.0547 \text{ \AA}^{-3}$ , respectively in the solid and liquid at its melting point  $T_M = 970$  K, giving rise to a density change of  $0.004 \text{ \AA}^{-3}$ . These values compare well to the respective experimental values [79, 99, 100] of  $0.0573 \text{ \AA}^{-3}$  and  $0.05306 \text{ \AA}^{-3}$  with a density change of  $0.0042 \text{ \AA}^{-3}$ . At the experimental melting temperature, the calculated density change remains essentially unchanged, and the densities in both phases deviate only by 2% with respect to the measurements.

### C. Liquid-solid interfaces

Liquid-solid interface (LSI) simulations are performed for the purpose of determining the melting line by the two-phase coexistence. The procedure follows the approaches proposed in Refs. [89–91, 104–109] and is similar to the protocol used in Ref. [24]. A simulation cell containing around  $N = 43000$  atoms is set up with an initial crystalline configuration with a shape corresponding to  $28 \times 7 \times 7$  primitive cells on which PBC are applied to the three

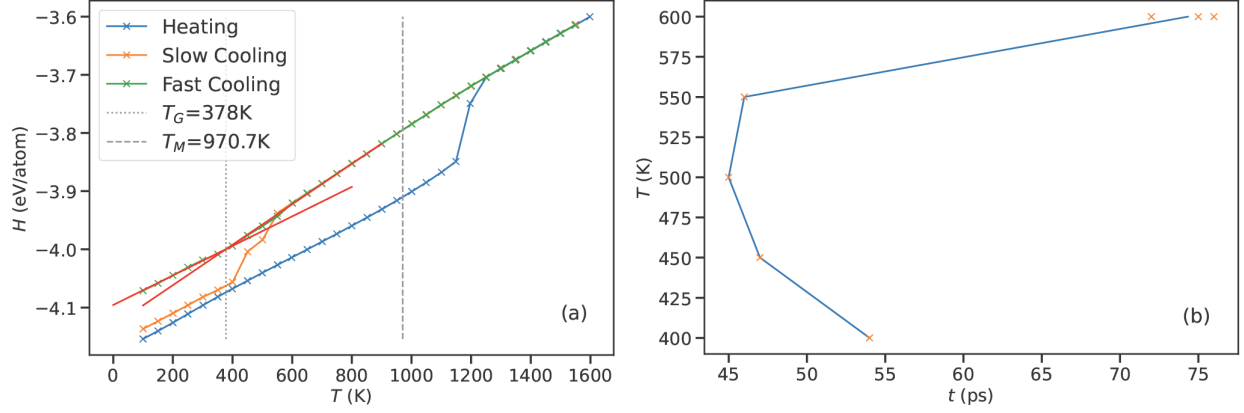


FIG. 7. (a) Enthalpy as a function of temperature for the solid (from heating) and liquid branches (from cooling) at ambient pressure as described in the text. The red lines indicate the slope of the amorphous and the supercooled states as a guide for the eyes for the crossover between the liquid and amorphous regimes, and marked by the vertical dotted line. The vertical dashed line marks the melting temperature obtained from the the LSI simulations. (b) The TTT curve, as described in the text. The orange crosses are individual measurements of the time it takes to reach 40% solidification, with the blue line connecting the averages for each temperature.

directions of space. Starting at zero pressure, this system is heated and equilibrated at constant pressure to a temperature of 50 K below a guess of the melting temperature. Half of the simulation cell in the  $x$  direction is further heated and maintained at a much higher temperature until a complete melting is observed. The liquid part is then cooled down and equilibrated at a temperature 50 K above the guess, thus creating a solid-liquid coexistence containing two crystal-melt interfaces due to the PBC. The simulation of the entire system is pursued in the isobaric-isoenthalpic ensemble so that the temperature of the LSI is an internal parameter free to evolve toward a steady state corresponding to the thermodynamic melting temperature if both phases survive. The simulation is continued for 1 ns, and the average melting temperature is determined on the last 100 ps when a steady position of the two interfaces is observed. If a complete melting or solidification occurs, the procedure is started over again with a refined guess of the melting temperature. This procedure is repeated with subsequent higher pressures by first shrinking the volume of the whole simulation cell from

the coexistence configuration at the preceding pressure and then increasing the temperature at constant pressure to a new guess of the melting line.

The melting curve of aluminium was measured [101, 102] up to 80 GPa using diamond anvil cells (DAC) and even higher at 125 GPa by means of shock experiments [103]. In Fig. 8, the results obtained from the HDNN are compared to these experimental data [101–103], the *ab initio* based equation of states (EOS) [83] as well as the AIMD two-phase approach [110] for which the GGA for the XC functional and 512 atoms were used. At ambient pressure, the HDNN potential yields a value of  $T_M = 970$  K which overestimates the experimental one of 933 K by 5%. This is also the case for the AIMD [110] to a lesser extent, recalling that the GGA was used and overestimates the atomic volume [81, 110]. With increasing pressure, the melting curve from the HDNN potential slightly underestimates the experiments as well as the EOS. By using two different sizes and shapes, negligible influence on the determination of the melting curve was found, confirming earlier results on pure Zr [24]. Noticeably, the reliability of the present potential on the melting line up to 200 GPa is then assessed, even if high pressure thermodynamic states included in the training set are really scarce. Interestingly, the HDNN curve is similar to the one obtained with the ANI-Al ML potential by Smith *et al.* [47], and even gives slightly better results at high pressure.

#### D. Homogeneous Nucleation

Finally, the homogeneous nucleation is investigated and depicted in Fig. 9. As pointed out in our preceding in our preceding work [24], a more accurate investigation require the use of large enough simulation boxes, with typically 1 million atoms or more. This allows the occurrence of multiple nuclei during the nucleation process. Therefore, the system of 1000188 atoms at ambient pressure is analyzed further along the 600 K isotherm used for the determination of the TTT curve in 7(b). At such a high degree of undercooling  $\Delta T = (T_M - T)/T_M = 0.38$ , an extremely fast nucleation process is observed [97, 98]. Similarly, such a fast homogeneous nucleation is seen at the high pressure of 200 GPa along the 4000 K with  $\Delta T = 0.24$ . Inherent structure configurations shown in Figs. (c)-(j) were first analyzed using the common-neighbor analysis [93] and only atoms with a crystalline



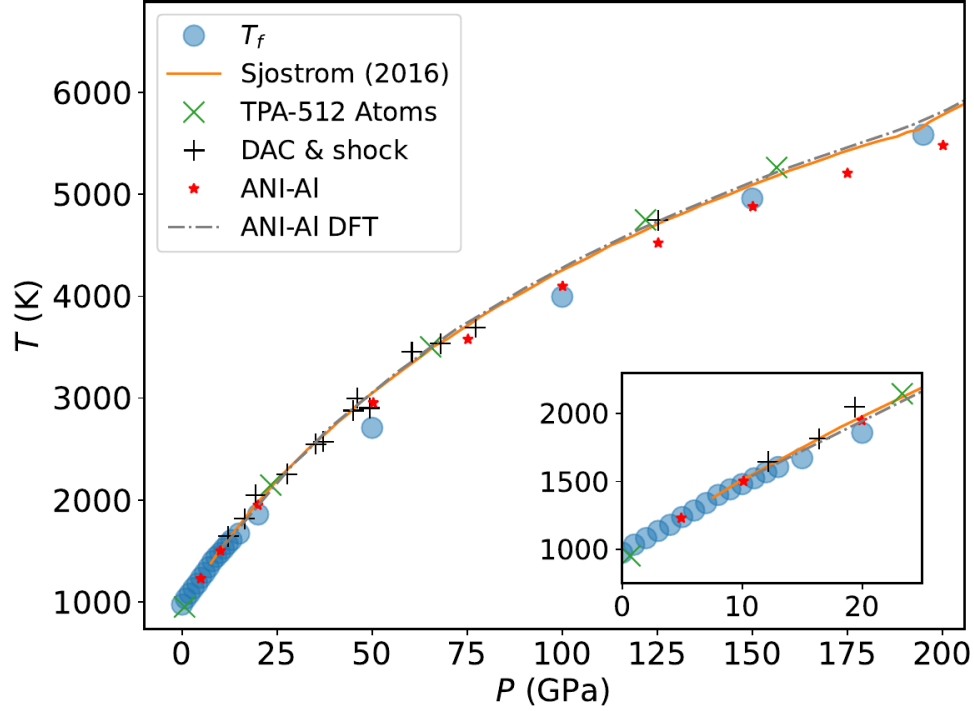


FIG. 8. Melting curve for aluminium as a function of pressure. The blue circles obtained from our LSI simulations with the HDNN are compared to the experimental data [101–103], the AIMD two-phase approach [110], and the ANI-AI ML potential [47]. The Inset highlights the lower pressure range up to 25 GPa.

environment (fcc, hcp, and bcc) are shown. As expected, nucleation occurs showing growing nuclei in the fcc ordering with hcp stacking faults at ambient pressure. At 200 GPa, nucleation starts with nuclei having a bcc order with sometimes some fcc ordering at their boundary that transform back to the bcc structure during the growth. These nucleation pathways are pretty much consistent with the  $(P, T)$  phase diagram [83] showing the reliability of the HDNN potential designed here.

The onset of nucleation occurs at about 30 ps at ambient pressure and 4 ps at 200 GPa, earlier than the nucleation time defined for the construction of the TTT curve above. Using the averaged Steinhardt Order Parameters  $q_4$  and  $q_6$  [111], embryos with atoms having a crystalline ordering showed that they dissolve back to the liquid with a size less than 90 atoms in both cases. The latter value does not represent *per se* the size critical nucleus but

rather a lower limit. As expected at ambient pressure, the main crystalline phase during the growth was identified as fcc, as can be seen in Fig. 10(a), but a significant hcp ordering also appears during the nucleation and remains as stacking fault after complete solidification of the simulation box as shown in Fig. 9. At high pressure, the onset of nucleation occurs in the bcc ordering, with fcc and hcp ordering at their surface at later stages.

It is an open question in general, whether the homogeneous nucleation process follows the Landau Theory in which the bcc precursor is favored in the early stages of crystal nucleation [112] or the Ostwald step rule [113] according to which a primary crystal phase could be different from the the fcc one. From the distributions of the  $q_6$  and  $q_4$  shown in Figs. 10(b) and 10(c) only fcc ordering emerges at the onset of nucleation. Our findings show that aluminium follows a single step process with an onset of homogeneous nucleation showing emerging embryos with a fcc ordering. The resulting nuclei grow in a rather patchy shape with a small amount of hcp stacking fault defects. This nucleation the scenario is different from the Lennard-Jones case [114, 115] which follows the Landau theory and the Ostwald step rule. The present large-scale molecular dynamics results with close *ab initio* accuracy allows us to assess very recent molecular dynamics simulations [3, 117] with EAM empirical potentials. Our findings further show that such a single step nucleation pathway also occurs at high pressure with bcc ordering in the emerging nuclei.

#### IV. CONCLUSION

In the present work, a machine learning potential for pure aluminium by means of a high dimensional neural network on the basis of the well-known Behler-Parrinello approach [35, 40] was developed. This ML potential is devoted to the description of condensed phases, namely liquid and solid states at ambient pressure as well as those at pressures up to 300 GPa with resulting temperatures as high as 8000 K. A crucial point was the training of the potential with a data set generated by DFT-based simulations not only to cover the targeted domain of thermodynamic states for a question of transferability but also to consider for each of them in a physical meaningful manner the time fluctuations by an appropriate sampling of phase space trajectories obtained by *ab initio* molecular dynamics. This allows to include

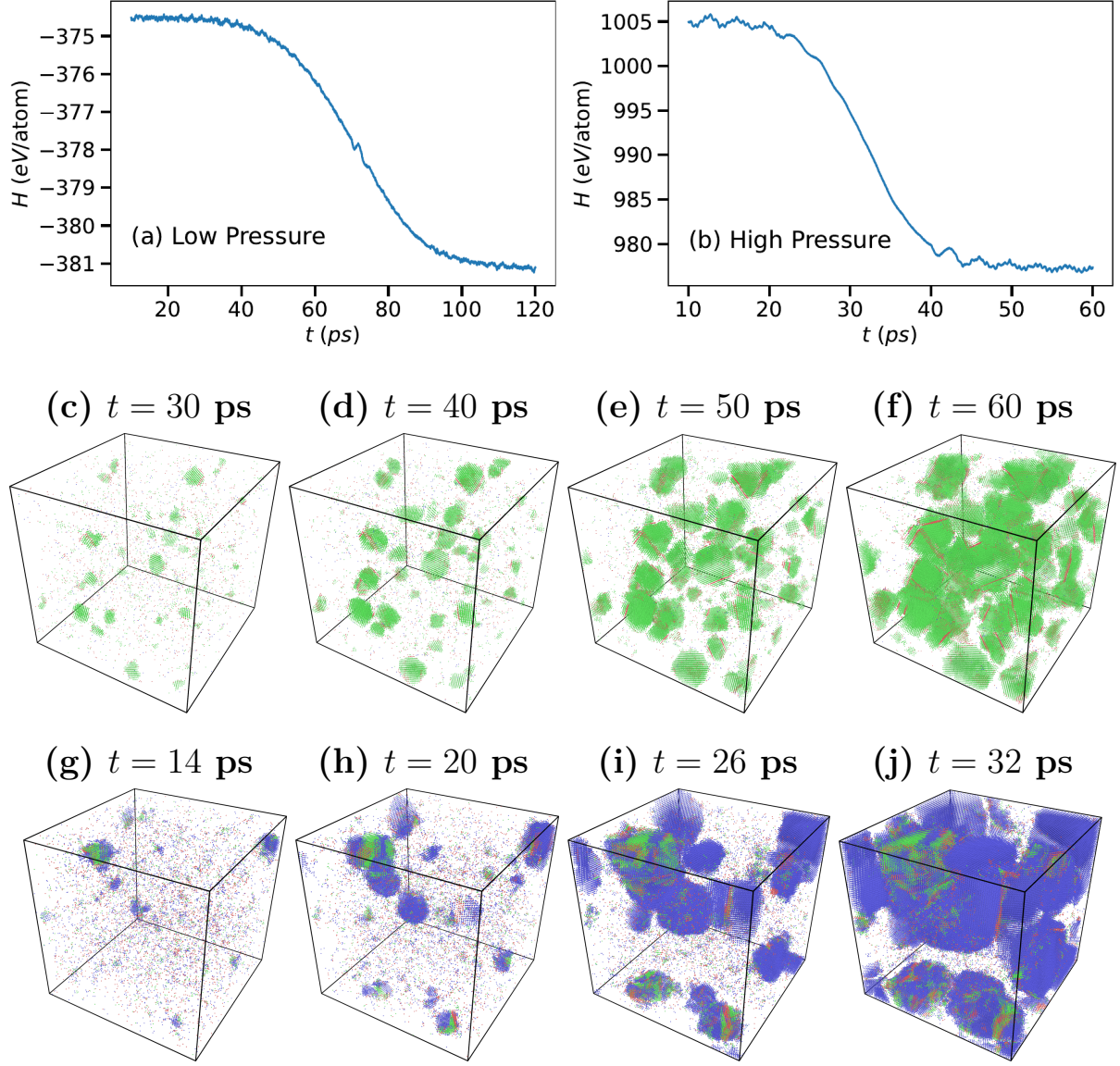


FIG. 9. Homogeneous nucleation of deeply undercooled aluminium along the  $T = 600$  K and 4000 K isotherms, respectively for ambient pressure and 200 GPa. Time evolution of the enthalpy (a) at ambient pressure, and (b) at 200 GPa. Snapshots of the simulation at various times during the nucleation (c) to (f) at ambient pressure, and (g) to (j) at 200 GPa. Only the atoms with crystalline ordering in the sense of the common-neighbor analysis are drawn: fcc (green); hcp (red); bcc (blue).

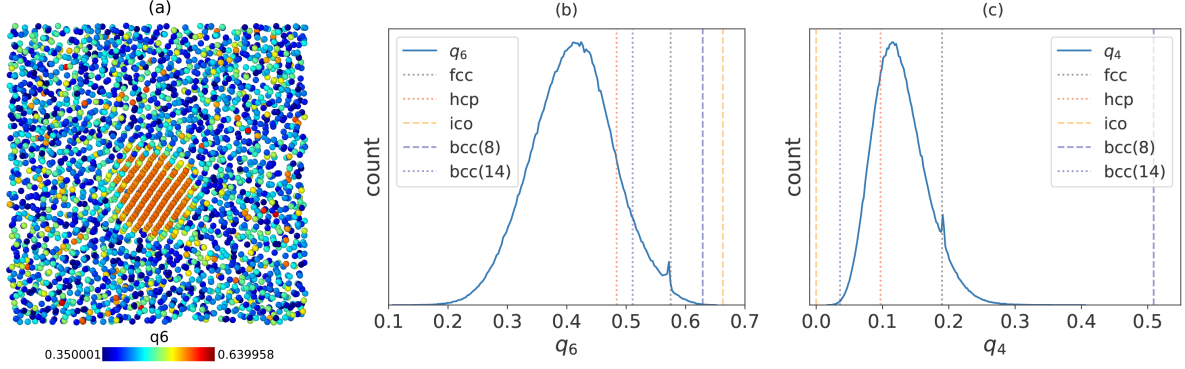


FIG. 10. (a) First identified nucleus at the onset of nucleation in a small box extracted from the snapshot at 30 ps (Fig. 9) for ambient pressure. Atoms are colored according to the value of the  $q_6$  averaged Steinhardt order parameter. (b-c) Corresponding histograms for all atoms in the simulation box of the  $q_6$  and  $q_4$  parameters showing clearly that nucleation starts with only a fcc ordering.

in the training the relevant accessible microstates of the considered thermodynamic states. Another approach based on metadynamics was shown to be efficient in selecting the relevant configurations to train the neural network [6].

The HDNN potential thus obtained was shown to be efficient in reproducing the structural, dynamics as well as thermodynamic quantities in the liquid, undercooled and crystalline states at ambient pressures as well as in the liquid state at high pressure up to 300 GPa, including the melting line. One important outcome is that a reliable ML potential could be obtained without including explicitly the forces in the training by using an appropriate sampling of AIMD trajectories. The procedure was shown for Al and HDNN to perform well, giving a RMSE on forces similar to what is currently obtained. The early stages of the homogeneous crystal nucleation were further investigated on a scale much larger than what is possible from the *ab initio* molecular dynamics but with a similar accuracy. Results show that aluminium follows a single step nucleation process with an emerging fcc ordering and hcp stacking fault defects, confirming recent works using large scale molecular dynamics [3, 117], and also consistent with very recent simulations on nucleation during cooling [118]. A single step nucleation pathway with bcc nuclei is also observed at high pressure.

Finally, the fact that the HDNN potential keeps a good accuracy even in domains where the thermodynamic states in the training set are scarce opens up a research line based upon active learning for regression approaches to reduce efficiently the training set. Dynamical properties such as the diffusion coefficients considered here are sensitive to the details of the potential and should be introduced in the training procedure in a more direct way than through the choice of the XC functional in the DFT calculations. This would represent a real step forward in designing ML potentials.

## ACKNOWLEDGMENTS

We acknowledge the CINES and IDRIS under Project No. INP2227/72914, as well as CIMENT/GRICAD for computational resources. This work was performed within the framework of the Centre of Excellence of Multifunctional Architected Materials “CEMAM” ANR-10-LABX-44-01 funded by the “Investments for the Future” Program. This work has been partially supported by MIAI@Grenoble Alpes (ANR-19-P3IA-0003). Fruitful discussions within the French collaborative networks in high-temperature thermodynamics GDR CNRS 3584 (TherMatHT) and in artificial intelligence in materials science GDR CNRS 2123 (IAMAT) are also acknowledged. We thank J. Smith and K. Barros for their kind help in setting up the simulations with their ANI-1 potential from Ref. [47]. J. S. acknowledges funding from the German Academic Exchange Service (DAAD) through the DLR-DAAD programme, grant No. 509.

- 
- [1] J. R. Davis, *Aluminum and Aluminum Alloys*, ASM International, p351, (2001).
  - [2] J. Hafner J. Comput. Chem. **29** 2044 (2008).
  - [3] C. P. Royall and S. R. Williams, Phys. Rep. **560**, 1 (2015).
  - [4] , K. F. Kelton A. L. Greer, *Nucleation in Condensed Matter: Applications in Materials and Biology* (Pergamon, 2010).
  - [5] N. Jakse and A. Pasturel, Phys. Rev. Lett. **99**, 2 (2007).

- [6] L. Bonati and M. Parrinello, Phys. Rev. Lett. **121**, 265701 (2018).
- [7] M. C. Payne, M. P. Teter, D. C. Allan, T. Arias, and J. Joannopoulos, Rev. Mod. Phys. **64**, 1045 (1992).
- [8] K. Burke, J. Chem. Phys. **136**, 150901 (2012).
- [9] R. Car and M. Parrinello, Phys. Rev. Lett. **55**, 2471 (1985).
- [10] N. Jakse and A. Pasturel, Sci. Rep. **3**, 3135 (2013).
- [11] A. Pasturel and N. Jakse, J. Appl. Phys. **123**, (2018).
- [12] Sosso, G. C. *et al.*, Chem. Rev. **116**, 7078 (2016).
- [13] J. Hafner, *From Hamiltonians to Phase Diagrams* (Springer-Verlag Berlin Heidelberg, 1987).
- [14] D. K. Belashchenko, Physics-Uspekhi **56**, 1176 (2013).
- [15] N. W. Ashcroft Pkys. Lett. **23** 48 (1966).
- [16] I. M. Wills and W. A. Harrison, Pkys. Rev. B **28** 4363 (1983).
- [17] J. A. Moriarty, Pkys. Rev. B **42** 1609 (1990).
- [18] N. Jakse and J.-L. Bretonnet, J. Phys.: Condens. Matter **7**, 3803 (1995).
- [19] M.S. Daw and M.I. Baskes, Phys. Rev. B **29**, 6443 (1984).
- [20] M.S. Daw, S.M. Foiles, M.I. Baskes, Mater. Sci. Rep. **9**, 251 (1993).
- [21] M.I. Baskes, Phys. Rev. B **46**, 2727 (1992).
- [22] H. S. Huang, L. Q. Ai, A. C. T. van Duin, M. Chen, and Y. J. Lü, J. Chem. Phys. **151**, 094503 (2019).
- [23] D.G. Pettifor, *Bonding and Structure of Molecules and Solids* (Oxford University Press, Oxford, 1996).
- [24] S. Becker, E. Devijver, R. Molinier, and N. Jakse, Phys. Rev. B **102**, 104205 (2020).
- [25] H. Zong, G. Pilania, X. Ding, G. J. Ackland, and T. Lookman, npj Comput. Mater. **4**, 48 (2018).
- [26] A. M. Goryaeva, C. Lapointe, C. Dai, J. Dérès, J.-B. Maillet, and M.-C. Marinica, Nat. Commun. **11**, 4691 (2020).
- [27] J. Behler, Int. J. Quantum Chem. **115**, 1032 (2015).
- [28] J. Behler, J. Chem. Phys. **145**, 170901 (2016).

- [29] R. Ramprasad, R. Batra<sup>1</sup>, G. Pilania, A. Mannodi-Kanakkithodi, and C. Kim, npj Comput. Mater. **3**, (2017).
- [30] J. Schmidt, M. R. G. Marques, S. Botti, and M. A. L. Marques, npj Comput. Mater. **5**, 83 (2019).
- [31] A. M. Goryaeva, J. B. Maillet, and M. C. Marinica, Comput. Mater. Sci. **166**, 200 (2019).
- [32] T. Mueller, A. Hernandez, and C. Wang, J. Chem. Phys. **152**, (2020).
- [33] M. R. G. Marques, J. Wolff, C. Steigemann and M. A. L. Marques, Phys. Chem. Chem. Phys. **21**, 6506 (2019).
- [34] A. Singraber T. Morawietz, J. Behler, and Christoph Dellago, J. Chem. Theory Comput. **15**, 3075 (2019).
- [35] A. Singraber, J. Behler, and C. Dellago, J. Chem. Theory Comput. **15**, 1827 (2019).
- [36] A. P. Thompson *et al.*, Comp. Phys. Comm. **271**, 108171 (2022); <http://www.lammps.sandia.gov>.
- [37] A. H. Larsen, J. J. Mortensen, J. Blomqvist, I. E. Castelli, R. Christensen, M. Dulak, J. Friis, M. N. Groves, B. Hammer, C. Hargus, E. D. Hermes, P. C. Jennings, P. B. Jensen, J. Kermode, J. R. Kitchin, E. L. Kolsbjerg, J. Kubal, K. Kaasbjerg, S. Lysgaard, J. Bergmann Maronsson *et al.*, J. Phys. Condens. Matter **29**, 273002 (2017).
- [38] Z. Li, J.R. Kermode, A. De Vita, Phys. Rev. Lett. **114**, 096405 (2015).
- [39] R. Jinnouchi, F. Karsai, and G. Kresse, Phys. Rev. B **100**, 014105 (2019).
- [40] J. Behler and M. Parrinello, Phys. Rev. Lett. **98**, 146401 (2007).
- [41] A. P. Bartók, G. Csányi, Int. J. Quantum Chem. **115**, 1051 (2015).
- [42] A. Thompson, L. Swiler, C. Trott, S. Foiles, G. Tucker, J. Comp. Phys. **285**, 316 (2015).
- [43] A. P. Bartók, M. C. Payne, R. Kondor, and G. Csányi, Phys. Rev. Lett. **104**, 136403 (2010).
- [44] V. Botu, R. Batra, J. Chapman, R. Ramprasad, J. Phys. Chem. C **121**, 511 (2017).
- [45] G. C. Sosso *et al.*, Phys. Rev. B - Condens. Matter Mater. Phys. **86**, 1 (2012).
- [46] T. Morawietz *et al.*, Proc. Natl. Acad. Sci. U. S. A. **113**, 8368 (2016).
- [47] J. S. Smith *et al.*, Nature Comm. **12**, 1257 (2021).
- [48] A. Pasturel and N. Jakse, npj Computational Materials **3**, 33 (2017).
- [49] J. Russo and H. Tanaka. J. Chem. Phys. **145**, 211801, (2016).

- [50] I. Kruglov, O. Sergeev, A. Yanilkin, and A. R. Oganov, *Sci. Rep.* **7**, (2017).
- [51] A. S. Bochkarev, A. van Rookeghem, S. Mossa, and N. Mingo, *Phys. Rev. Mater.* **3**, 093803 (2019).
- [52] L. A. Girifalco, and V. G. Weizer, *Physical Review*, **114**, 687 (1959).
- [53] K. W. Jacobsen, J. K. Norskov, and M. J. Puska, *Physical Review B*, **35**, 7423 (1987).
- [54] J. Mei and J. W. Davenport, *Phys. Rev. B* **46**, 21 (1992).
- [55] F. Ercolessi, and J. B Adams, *Europhys. Letters* **26**, 583 (1994).
- [56] Y. Mishin, D. Farkas, M.J. Mehl, and D.A. Papaconstantopoulos, *Phys. Rev. B* **59**, 3393 (1999).
- [57] J. B. Sturgeon, and B. B. Laird (2000), *Phys. Rev. B* **62**, 14720 (2000).
- [58] B.-J. Lee, J.-H. Shim, and M. I. Baskes, *Phys. Rev. B*, **68**, 144112 (2003).
- [59] X.-Y. Liu, F. Ercolessi, and J. B. Adams, *Modell. Sim. Mat. Sci. Eng.*, **12**, 665 (2004).
- [60] E. B. El Mendoub, R. Albaki, I. Charpentier, J.-L. Bretonnet, J.-F. Wax, and N. Jakse, *J. Non-Crystal Solids* **353**, 3475 (2007).
- [61] M. I. Mendelev, M. J. Kramer, C. A. Becker, and M. Asta, *Philosophical Magazine*, **88**, 1723 (2008).
- [62] J. M. Winey, A. Kubota, and Y. M. Gupta, *Modell. Simul. Mat. Sci. Eng.* **17**, 055004 (2009).
- [63] V. V. Zhakhovskii, N. A. Inogamov, Y. V. Petrov, S. I. Ashitkov, and K. Nishihara, *Appl. Surf. Sci.*, **255**, 9592 (2009).
- [64] K. Choudhary, T. Liang, A. Chernatynskiy, Z. Lu, A. Goyal, S. R. Phillpot, and S. B. Sinnott, *J. Phys.: Condens. Matter*, **27**, 015003 (2015).
- [65] M.I. Pascuet, and J.R. Fernández J. *Nucl. Materials*, **467**, 229 (2015).
- [66] L. Zhang, J. Han, H. Wang, R. Car, and W. E, *Phys. Rev. Lett.* **120**, 143001 (2018).
- [67] T. Hastie, R. Tibshirani, and J. Friedman, *The Elements of Statistical Learning Data Mining, Inference, and Prediction*, 2nd Edition, Springer Series in Statistics (Springer 2008).
- [68] the Python package can be found here : <https://www.tensorflow.org>
- [69] O. T. Unke et al., *Chem. Rev.* **121**, 10142 (2021).
- [70] N. Jakse and A. Pasturel *J. Phys. Condens Matter* **25** 28510 (2013).
- [71] N. Jakse and T. Bryk, *J. Chem. Phys.* **151**, 034506 (2019).



- [72] F. Demmel, L. Hennet, and N. Jakse, Sci. Rep. (Nature) **11**, 11815 (2021).
- [73] G. Kresse and J. Furthmuller, Comput. Mater. Sci. **6**, 15 (1996).
- [74] D. M. Ceperley and B. J. Alder, Phys. Rev. Lett. **45**, 566 (1980).
- [75] J. P. Perdew and A. Zunger, Phys. Rev. B **23**, 5048 (1981).
- [76] G. Kresse and D. Joubert, Phys. Rev. B **59**, 1758 (1999).
- [77] H. J. Monkhorst and J. D. Pack, Phys. Rev. B **13**, 5188 (1976).
- [78] P. E. Blöchl, O. Jepsen and O. K. Andersen Phys. Rev. B **49**, 16223 (1994).
- [79] M. J. Assael, *et al.*, J. Phys. Chem. Ref. Data **35**, 285 (2006).
- [80] F. Demmel, D. Szubrin, W. C. Pilgrim, and C Morkel, Phys. Rev. B **84**, 014307 (2011).
- [81] D. Alfè, Phys. Rev. B **68**, 064423 (2003).
- [82] F. Kargl, H. Weis, T. Unruh, and A. Meyer, J. Phys.: Conf. Ser. **340**, 012077 (2012).
- [83] T. Sjostrom, S. Crockett, and S. Rudin, Phys. Rev. B **94**, 144101 (2016).
- [84] J. P. Perdew, J. A. Chevary, S. H. Vosko, K. A. Jackson, M. R. Pederson, D. J. Singh, and C. Fiolhais, Phys. Rev. B **46**, 6671 (1992).
- [85] D. J. Wales, Energy Landscapes (Cambridge University Press, 2003).
- [86] A. S. Christensen and O. A. von Lilienfeld, Mach. Learn. Sci. Technol. **1**, 045018 (2020).
- [87] M. P. Allen, D. J. Tildesley. *Computer simulation of liquids*, Oxford Science Publication (1989).
- [88] B. Smit and D. Frenkel. *Understanding molecular simulations*, 2nd ed., Academic Press, San Diego (2002).
- [89] D. Y. Sun, M. Asta, and J. J. Hoyt, Phys. Rev. B **69**, 024108 (2004).
- [90] J. R. Morris, C. Z. Wang, K. M. Ho, and C. T. Chan, Phys. Rev. B **49**, 3109 (1994).
- [91] J. R. Morris and X. Y. Song, J. Chem. Phys. **116**, 9352 (2002).
- [92] J. D. Honeycutt, and H. C. Andersen, J. Phys. Chem. **91**, 4950 (1987).
- [93] D. Faken and H. Jonsson. Comput. Mat. Sci. **2**. 279 (1994).
- [94] A. Stukowski, *Visualization and analysis of atomistic simulation data with OVITO - the Open Visualization Tool*, Modelling Simul. Mater. Sci. Eng. **18**, 015012 (2010).
- [95] K. Binder and W. Kob, *Glassy Materials and Disordered Solids* (World Scientific Publishing, Singapore, 2005).

- [96] N. A. Mauro, J. C. Bendert, A. J. Vogt, J. M. Gewin, and K. F. Kelton, J. Chem. Phys. **135**, 044502 (2011).
- [97] D. M. Herlach, S. Binder, P. Galenko, J. Gegner, D. Holland-Moritz, S. Klein, M. Kolbe, and T. Volkman, Metall. Mater. Trans. A Phys. Metall. Mater. Sci. **46**, 4921 (2015).
- [98] J. Orava and A. L. Greer, J. Chem. Phys. **140**, 214504 (2014).
- [99] M. Leitner et al., Metall. Mater. Trans. A Phys. Metall. Mater. Sci. **48**, 3036 (2017).
- [100] G. Simmons and H. Wang, Single Crystal Elastic Constants and Calculated Aggregate Properties. A Handbook 2nd Edition (The MIT Press, Cambridge, 2009).
- [101] R. Boehler and M. Ross, Earth Planet. Sci. Lett. **153**, 223 (1997).
- [102] A. Hännström and P. Lazor, J. Alloys Compd. **305**, 209 (2000).
- [103] J. W. Shaner, J. M. Brown, and R. G. McQueen, *High Pressure in Science and Technology* (North Holland, Amsterdam, 1984).
- [104] T. Zykova-Timan, R. E. Rozas, J. Horbach, and K. Binder, J. Phys.: Condens. Matter **21**, 464102 (2009).
- [105] T. Zykova-Timan, J. Horbach, and K. Binder, J. Chem. Phys. **133**, 014705 (2010).
- [106] P. Kuhn and J. Horbach, Phys. Rev. B **87**, 014105 (2013).
- [107] R. Benjamin and J. Horbach, J. Chem. Phys. **143**, 014702 (2015).
- [108] R. Rozas, A. Demirag, P. G. Toledo, and J. Horbach, J. Chem. Phys. **145**, 064515 (2016).
- [109] R. E. Rozas, L. G. MacDowell, P. G. Toledo, and J. Horbach, J. Chem. Phys. **154**, 184704 (2021).
- [110] J. Bouchet et al., Phys. Rev. B - Condens. Matter Mater. Phys. **80**, 1 (2009).
- [111] W. Lechner and C. Dellago, J. Chem. Phys. **129**, 114707 (2008)
- [112] Alexander, S. & McTague, J. P. Should all crystals be bcc? Landau theory of solidification and crystal nucleation. Phys Rev Lett **41**, 702–705 (1978).
- [113] Ostwald, W. The formation and changes of solids (Translated from German). Z. Phys. Chem. **22**, 289–330 (1897).
- [114] ten Wolde, P. R., Ruiz-Montero, M.J. and Frenkel D., Phys Rev Lett **75**, 2714–2717 (1995).
- [115] ten Wolde, P. R., Ruiz-Montero, M. J. & Frenkel, D. Numerical calculation of the rate of crystal nucleation in a Lennard-Jones system at moderate undercooling. J. Chem. Phys. **104**,

9932–9947 (1996).

- [116] Mahata, A., Zaeem, M. A. & Baskes, M. I. Understanding homogeneous nucleation in solidification of aluminum by molecular dynamics simulations. *Model. Simul. Mater. Sci. Eng.* **26**, (2018).
- [117] S. Becker, E. Devijver, R. Molinier, and N. Jakse, *Sci. Rep. (Nature)* **12** 3195 (2022).
- [118] L. Zhou et al., *RSC Adv.* **11**, 39829 (2021).

## Supplementary Information File

### V. DATASET FOR THE TRAINING OF THE HDNN POTENTIAL

Tables SII and SIII gather all thermodynamics states that have been simulated by AIMD to generates configuration for the training procedure of the HDNN potential. For each state, after an equilibration at a target temperature a phase space trajectory was produced from which a sample of configurations was randomly extracted to include in the data set. Additional AIMD at  $T = 950$  K and  $P = 0$  GPa, 1500 K and 2.5 GPa, 2000 K and 28 GPa, and 8000 K and 227 GPa were performed but were not included in the data set for the sake of testing the predictive ability of the HDNN potential. The database contains in total 24300, which amounts to 6 220 800 atoms.

### VI. EAM AND MEAM PAIR-CORRELATION FUNCTIONS

To get a sense of how our HDNNP compares to other widely used potentials, we have run simulations using the Embedded Atom Model (EAM) [2] and Modified Embedded Atom Model (MEAM) [1] potentials both known as performing well in the liquid and solid states (see Ref. [3] and references therein). These simulations were performed identically to the ones used to obtain the pair-correlation functions for our HDNNP, and for the same set of temperatures and densities (see the main text). Figure S11 shows  $g(r)$  obtained from these simulations, along with the corresponding AIMD ones. For the sake of clarity, the results of the HDNN potential are not shown since they match very closely the AIMD curves.

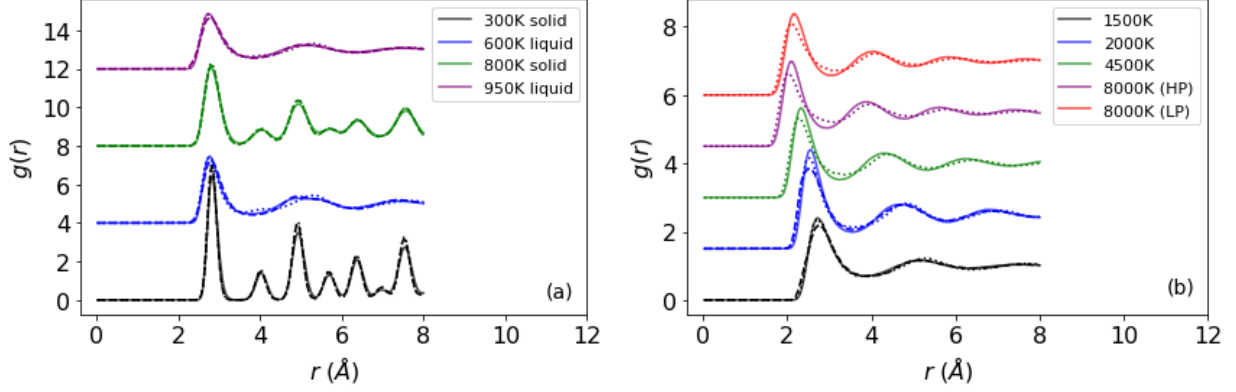


FIG. S11. Pair-correlation functions obtained using the Embedded Atom Model (dashed lines) and Modified Embedded Atom Model (dotted lines) potentials, with solid lines showing the corresponding  $g(r)$  obtained from AIMD simulations. Lines of same color correspond to the same temperature and system volume. The plots for  $T = 600, 800$ , and  $950$  K are shifted upwards by 4, 8, and 12. Likewise the plots for  $T = 2000, 4500, 8000$  K (HP), and  $8000$  K (LP) are shifted by 1.5, 3, 4.5, and 6. The two  $8000$  K lines correspond to high (360 GPa) and low (250 GPa) pressure.

It is worth mentioning that above 20 GPa we were not able to achieve MD simulations with the EAM potential. At ambient pressure, both EAM and MEAM reproduce well the AIMD simulations even if noticeable can be seen. At larger pressures and temperature the agreement worsen showing that the EAM is not transferable while the MEAM still gives reasonable results.

The mean square error between the two were calculated, as shown in table SIV. In this table, are given the  $p$ -values obtained by performing a  $t$ -test statistics between the square errors  $(g_{\text{AIMD}}(r) - g_{\text{NNP}}(r))^2$  and  $(g_{\text{AIMD}}(r) - g_{\text{emp.}}(r))^2$ , treating the error at different radii as independent.

## VII. STEINHARDT PARAMETER ANALYSIS

To study the local ordering before and during nucleation we have used the Steinhardt bond-ordering parameters[4], more specifically the averaged form[5], as implemented in the

Structure	$T$ (K)	$P$ (GPa)	Trajectory (ps)	Sample size
fcc	10	0	40	1000
fcc	300	0	40	1000
fcc	400	0	40	1000
fcc	500	0	40	1000
fcc	600	0	40	1000
fcc	700	0	40	1000
fcc	800	0	40	1000
fcc	10	1	10	100
fcc	10	10	10	100
fcc	10	100	10	100
hcp	10	0	10	100
hcp	10	10	10	100
hcp	10	100	10	100
hcp	10	200	10	100
hcp	10	300	10	100
bcc	10	0	10	100
bcc	10	10	10	100
bcc	10	100	10	100
bcc	10	200	10	100
bcc	10	300	10	100

TABLE SII. Characteristics of the data set built from AIMD simulations. Are given the structure of the simulation (fcc, hcp, bcc, and liquid), the temperature  $T$ , the pressure  $P$ , the time span of the AIMD trajectory from which the configuration are sampled, the sample size, namely the number of configurations randomly extracted from the trajectory. The pressures less than 1 GPa were indicated as 0.

Structure	$T$ (K)	$P$ (GPa)	Trajectory (ps)	Sample size
Liquid	500	0	40	1000
Liquid	600	0	40	1000
Liquid	650	0	40	1000
Liquid	700	0	40	1000
Liquid	750	0	40	1000
Liquid	800	0	40	1000
Liquid	1000	0	40	1000
Liquid	1100	0	40	1000
liquid	1250	0	40	1000
liquid	1350	0	40	1000
liquid	1500	0	40	1000
liquid	1600	0	40	1000
liquid	1700	0	40	1000
liquid	3100	56	40	1000
liquid	4500	107	40	1000
liquid	8000	320	40	1000

TABLE SIII. Characteristics of the data set built from AIMD simulations (ontinued). Same caption as Table SII.

pyscal code[6]. First define for each atom  $i$  the vector

$$q_{lm}(i) = \frac{1}{N(i)} \sum_{j=1}^{N(i)} Y_{lm}(\mathbf{r}_{ij}) \quad (6)$$

where  $N(i)$  is the number of nearest neighbors of atom  $i$ ,  $\mathbf{r}_{ij}$  is the displacement of nearest-neighbor atom  $j$  from  $i$ , and  $Y_{lm}$  is the spherical harmonics. From these the averaged bond-order parameters can be defined as

$$\bar{q}_l(i) = \sqrt{\frac{4\pi}{2l+1} \sum_{m=-l}^l \left| \frac{1}{N(i)+1} \sum_{k=0}^{N(i)} q_{lm}(k) \right|^2} \quad (7)$$

$T$ (K)	300	600	800	950
MSE (EAM)	0.0297	0.0041	0.0048	0.0032
MSE (MEAM)	0.036	0.0065	0.0064	0.0018
$p$ (EAM)	$5.49 \times 10^{-6}$	$3.59 \times 10^{-4}$	$4.48 \times 10^{-6}$	$3.71 \times 10^{-6}$
$p$ (MEAM)	$5.48 \times 10^{-7}$	$2.20 \times 10^{-13}$	$3.98 \times 10^{-9}$	$3.78 \times 10^{-10}$

$T(K)$	1500	2000	4500	8000 (H)	8000 (L)
MSE (EAM)	0.0028	0.012	N/A	N/A	N/A
MSE (MEAM)	0.00086	0.066	0.0091	0.015	0.0095
$p$ (EAM)	$4.24 \times 10^{-5}$	$1.51 \times 10^{-6}$	N/A	N/A	N/A
$p$ (MEAM)	$5.96 \times 10^{-7}$	$9.63 \times 10^{-16}$	$1.04 \times 10^{-11}$	$7.44 \times 10^{-11}$	$5.92 \times 10^{-11}$

TABLE SIV. Mean-square error of the pair-correlation function  $g(r)$  obtained *via* the EAM and MEAM potentials, and evaluated against the one obtained from AIMD, with corresponding  $p$ -values (noted here as  $p$ ) as explained in the text.

where the sum from  $k = 0$  to  $N(i)$  includes both the atom  $i$  and its nearest neighbors. Due to being averaged over nearest neighbors, these parameters take into account not just the first coordination shell, but also the second. To perform structural analysis using these parameters one typically selects specific values for  $l$ , with  $l = 4$  and  $l = 6$  being a common choice. It is then possible to compare the resulting values of  $\bar{q}_l$  to those of ideal crystals in order to identify crystal structure.

- 
- [1] B.-J. Lee, J.-H. Shim, and M. I. Baskes, Phys. Rev. B, **68**, 144112 (2003).
  - [2] M. I. Mendelev, M. J. Kramer, C. A. Becker, and M. Asta, Philosophical Magazine, **88**, 1723 (2008).
  - [3] Mahata, A., Zaeem, M. A., and Baskes, M. I. Model. Simul. Mater. Sci. Eng. **26**, (2018).
  - [4] P. Steinhardt, D. R. Nelson, and M. Ronchetti, Phys. Rev. B, **28**, 784 (1983)

- [5] W. Lechner, C. Dellago, J. Chem. Phys., **129**, 114707 (2008)
- [6] S. Menon, G. D. Leines, and J. Rogal, J. Open Source Softw., **4(43)**, 1824 (2019)